Modelling verification and influence of operational patterns on tribological behaviour of wheel-rail interaction

Ma, Yuewei; Markine, Valeri; Mashal, AA; Ren, M

DOI
10.1016/j.triboint.2017.04.038

Publication date
2017

Published in
Tribology International

Modelling verification and influence of operational patterns on tribological behaviour of wheel-rail interaction

Yuewei Ma[1], Valeri Markine[1], Abdul Ahad Mashal[1], Mingfa Ren[2]

1. Section of Railway Engineering, Faculty of Civil Engineering and Geosciences, Delft University of Technology, Stevinweg 1, 2628CN, Delft, The Netherlands

2. State Key Laboratory of Structural Analysis for Industry Equipment, Dalian University of Technology, Dalian, 116024, China

Abstract

Verification of the explicit finite element (FE) model with realistic wheel-rail profiles against the CONTACT model, which has not been sufficiently discussed, is performed by comparing the resulting shear stress, slip-adhesion area, etc., obtained from the two models. The follow-up studies using the verified FE model on the influence of the varying operational patterns (such as different friction, traction, etc.) on the surface and subsurface tribological responses of wheel-rail interaction are accomplished through a series of simulations. It can be concluded that the results obtained from most of the explicit FE simulations agree reasonably well with the ones from CONTACT. Also, the increase of the friction and traction can bring the stress concentrations from the subsurface upwards to the surface.

Keywords: Wheel-rail interaction; Tribological behaviour; CONTACT; FE modelling verification;

1 Introduction

With the growing power of modern computers, expectations of more accurate contact models for the analysis of wheel-rail interaction have also been increased. Those models without validation or verification may generate subtle inaccuracy in the obtained results that being unnoticed, which can lead to wrong decisions [1]. Accordingly, it brings the researchers a tough challenge to justify the obtained results. In order to critically assess the confidence in the solution of a contact problem, the verified and validated contact models/algorithms have always been in high demand. Usually, validation is defined as the assessment of the computational accuracy of the numerical simulations by comparing it with the experimental data [2], while verification is performed through the comparison of the numerical results with a known solution obtained from other validated/verified models. The major difference between verification and validation lies in the relationship between the computational and the real world results (experimental data).

During the last decades, the interest in verification and validation of numerical models in the railway community has significantly been increased [3-11]. Usually, the validation is more difficult to perform than the verification, as the experimental methods [4, 7, 10, 11] are inherently more time consuming and expensive. Moreover, there are no well-accepted experimental methods available that can directly measure the intangible local stresses and micro-slips within the contact patches [8]. A common way of verifying a contact model is to compare its results with those from more rigorous models, of which the correctness and

accuracy have been proven [12]. For example, the Kalker's exact theory implemented in his well-known computer programme CONTACT is often used for this purpose. Zhao et al. [8] developed a three dimensional (3D) wheel-rail finite element model for the solution of rolling contact in elasticity and plasticity. Both the resulting Hertzian normal and tangential solutions agree quite well with the results from CONTACT. As Zhao's model was intended for studying squats that are usually found in the middle of rail top [13], it was reasonable to represent the wheel by a cylinder. Deng et al. [9] made attempts to find the solution for spin-rolling contact with a coned wheel tread. The obtained FE results were successfully verified against Kalker's exact theory (CONTACT). In [5], Vo et al. used both CONTACT [12] and Polach's models [14, 15] to verify the accuracy of their FE model through the comparison of contact forces. Both realistic rail and wheel profiles were considered in Vo's FE model. The comparison of the contact properties such as normal pressure, shear stress, slip-adhesion area, etc. with the ones of CONTACT was excluded. Wiest et al. [16] compared the normal contact pressure obtained from their FE simulations on wheel-crossing interaction with the ones from CONTACT. A novel coupling procedure between multibody system software and FE programme was introduced. Using that procedure, the conventional complete wheel-crossing dynamic FE model is able to be simplified into a static sub-model with two small pieces (around 30mm thick) of the contact bodies considered. The normal contact pressure in wheel-crossing contact is assessed and further verified against CONTACT.

From this literature review it can be noticed that despite the significant progress in the verification of FE contact models against CONTACT, verification of the models with realistic wheel and rail profiles has not sufficiently been performed. Therefore, the examination on the validity of FE contact models with realistic contact geometries remains in high demand. Also, the follow-up parametric studies on the influence of the operational patterns (such as the variation of friction coefficient [17-19], traction force [20], contact point [21] etc.) on the tribological behaviour of wheel-rail interaction are limited by the lack of reliable and justified FE models.

In this study, the explicit finite element model of a wheel rolling over a rail that uses a novel adaptive mesh refinement procedure coupled with two dimensional (2D) geometrical contact analysis is used. The main objectives of this study are to verify the developed FE model against CONTACT software and to explore the effect of the most influencing factors on the tribological behaviour of wheel-rail interaction through parametric studies using this model. The paper is organized as follows. In Section 2, a brief overview of the developed explicit finite element model is given. The comparison between the results obtained using the FE model and CONTACT is highlighted in Section 3. Following that, the results of the parametric studies on the influence of the friction coefficient, traction force, contact point, material properties, etc., on the tribological responses of wheel-rail interaction are presented in Section 4; The future work on the experimental validations and further applications of the developed FE model are discussed in Section 5; Finally, concluding remarks are presented in Section 6.

2 Wheel and rail 3D explicit FE model

In this section, the FE model for the analysis of the wheel and rail interaction is presented.

The main components of the model are shown in Figure 1. The model consists of the wheel with the standard S1002 profile and the standard 54E1 rail. Note that the model can easily be adjusted for other wheel and rail profiles.

The rail modelled with restriction to an overall length of 1.8m, is adopted by taking advantage of the symmetrical characteristic of the track and the wheelset. The wheel is set to roll from the origin of the global coordinate system $O-XYZ$ over a short travelling distance of 0.52m on the rail (See Figure 1a). The global coordinate system $O-XYZ$ is defined as: the Z-axis is parallel to the longitudinal direction along which the wheelset travels, the Y-axis is the vertical direction pointing upwards, and the X-axis is perpendicular both Y and Z directions, forming a right-handed Cartesian coordinate system.

Only the regions where the wheel travels are discretised with the dense mesh, leaving the remaining regions with the coarse mesh (See Figure 1a-d). The solution area is introduced and positioned in the middle of the dense mesh area. The solution area is defined as the region to extract and analyse the contact properties, such as the resulting contact patch, normal pressure, shear stress, etc. In this region, the mesh size (1mm) is approximately two times smaller than the dense mesh area (2mm) for the purpose of capturing the high stress/strain gradients inside the contact patch.

Table 1. Main parameters for the baseline verification case.

Properties		Values
Wheel/rail	Young's modulus (GPa)	210
	Passion ratio	0.3
	Density (kg/m^3)	7900
Primary suspension	Stiffness (MN/m)	1.15
	Damping (Ns/m)	2500
Operational parameters	Friction coefficient	0.5
	Traction coefficient	0.25
	Train velocities (km/h)	140
	Lateral Displacement (mm)	0.0
Track	Rail inclination	1/40

To take the primary suspension system into account, a group of sprung mass blocks are supported by the spring-damper elements. The mass blocks, which are used to represent the weight of the loaded car body, are 10 tons. The corresponding parameters of the springs and dampers are listed in Table 1. The linear elastic material models are used to describe the constitutive relation of the wheel and rail components [22].

In the explicit FE simulations (ANSYS LS-DYNA), the penalty method [23, 24] is used to enforce the contact constrains, where a list of invisible "interface spring" elements are placed between all the penetrating slave segments and the master segments (as depicted in Figure 1g-h). These contact segments are the nodes on the outmost surface layer of the wheel and rail contact bodies. The restoring interface force vector $\mathbf{f}$ is aligned with the normal of the master segment $\mathbf{n}$ and linearly dependent on the penetration depth l.

$$\mathbf{f} = -l \cdot k \cdot \mathbf{n} \quad if \ l < 0, \text{penetration occurred} \tag{1}$$

k represents the interface spring stiffness (See Figure 1h).

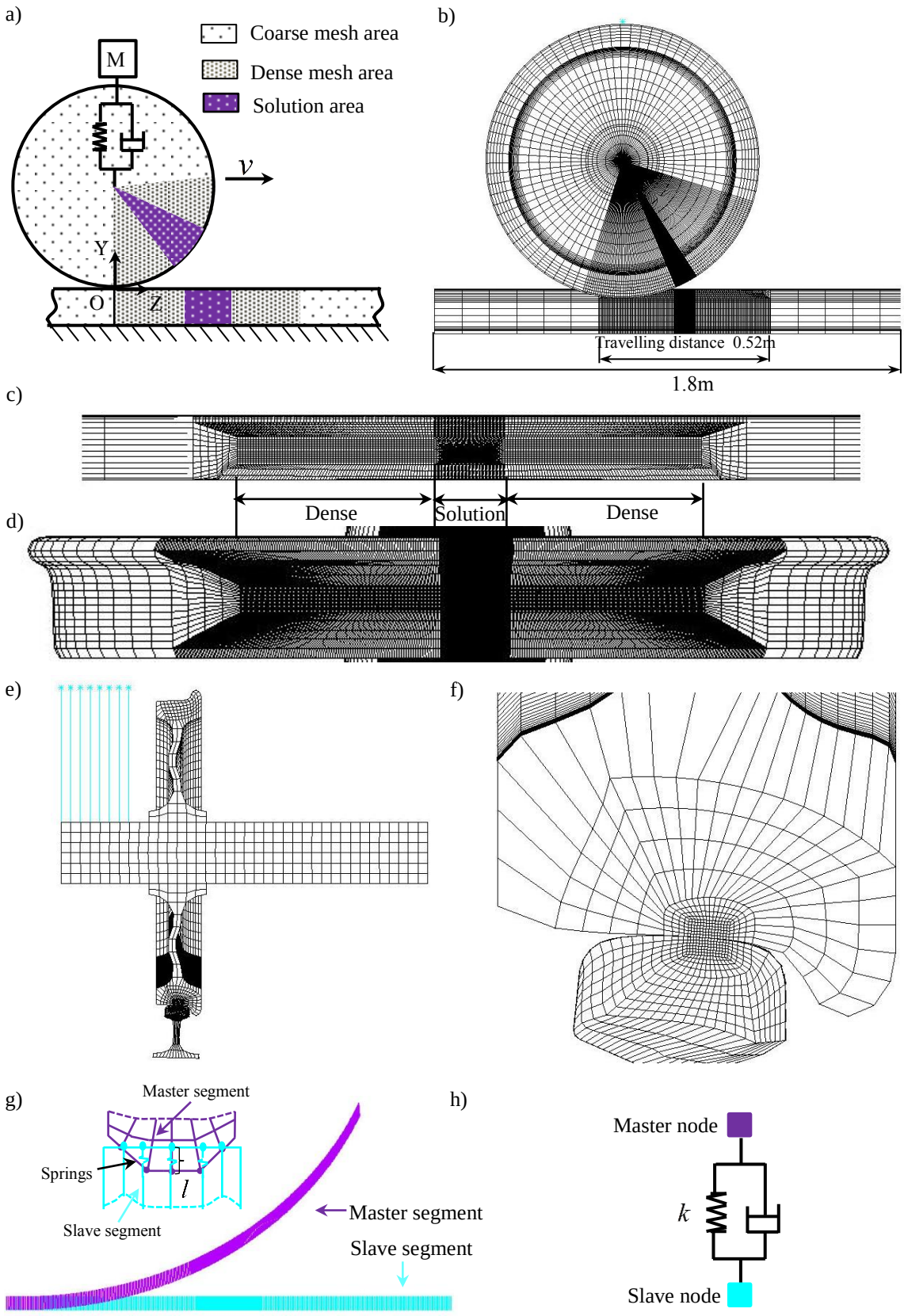

Figure 1. Wheel and rail dynamic contact model. a) Schematic diagram of FE model; b) FE model – side view; c) Nested mesh at rail refined region; d) Refined mesh at wheel potential contact area; e) FE model – cross sectional view; f) Close-up view in the refined contact region; g) Master-slave segments and schematic graph of its interaction; h) schematic of the invisible spring-damper contact element.

Friction in LS-DYNA is based on the Coulomb formulation [24, 25]. To predict the frictional force f^{n+1} at next time step t_{n+1}, a trail force f^* calculated based on the frictional force f^n at the present time step t_n is introduced in the friction algorithm [24, 25]:

$$f^* = f^n - k\Delta e \tag{2}$$

where Δe is the relative displacement increment. The next frictional force f^{n+1} is given as:

$$f^{n+1} = \begin{cases} f^* & if \left| f^* \right| \le F_{yield} \\ \dfrac{F_{yield} f^*}{\left| f^* \right|} & if \left| f^* \right| > F_{yield} \end{cases} \tag{3}$$

where F_{yield} refers to the maximum possible friction force $\mu|\mathbf{f}|$. As the simulation starts, the explicit FE programme predicts the frictional force iteratively using the central difference method [24].

The present FE model has 274,022 elements and 286,896 nodes. All the explicit FE simulations are performed on a workstation with an Intel(R) Xeon(R) @ 3.10 GHz 16 cores CPU and 32GB RAM. Also, the shared memory parallel processing capability of ANSYS LS-DYNA (High Performance Computation module) for 8 processors is used. Each simulation takes around 9 hours. The result file is approximately 45 GB.

3 Modelling verification

To properly verify the results from the proposed FE model analysis against the ones of CONTACT analysis, a physical understanding on the background of CONTACT is necessary. Thus, some critical theoretical backbones of CONTACT are summarised first. Then, the procedure to perform the verification that integrates the CONTACT model with the developed FE model is demonstrated. Finally, the simulation results obtained using the FE model are compared with the CONTACT results.

3.1 CONTACT model

The CONTACT programme is developed by Professor J.J. Kalker [26] and powered by VORtech Computing [27]. It is intended for treating the concentrated contact problems between two deformable bodies, which are assumed to have contact at one point O_c in the un-deformed state as shown in Figure 2. As one main function of CONTACT programme, it is able to accurately estimate the actual contact area A_C, the resulting local stresses and slips within the contact patch in the deformed state(i.e. when the wheel is shifted downwards to the rail along the direction O_cY_c).

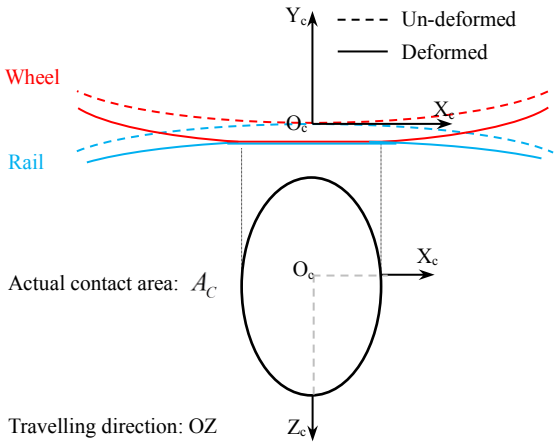

Figure 2 Schematic diagram of wheel-rail interaction in CONTACT (adapted from [28]).

CONTACT is based on the complementary energy principles of Fichera and Duvaut-lions [29], which are implemented in a special algorithm by Kalker [30]. In addition, the relations between the displacement $\mathbf{u}(\mathbf{x},t)$ and the surface traction $\mathbf{p}(\mathbf{x}',t)$ are defined as [27]

$$\mathbf{u}(\mathbf{x},t)=\int_{\mathbf{x}\in A_C}\mathbf{A}(\mathbf{x},\mathbf{x}')\mathbf{p}(\mathbf{x}',t)dS. \tag{4}$$

where $\mathbf{A}(\mathbf{x},\mathbf{x}')$ is the influence function. The influence function is used to assess the effect of the surface traction $\mathbf{p}(\mathbf{x}',t)$ applied on one particle positioned at $\mathbf{x}'$ on the displacement $\mathbf{u}(\mathbf{x},t)$ of another particle placed at $\mathbf{x}$. In CONTACT, the following assumptions are made [27]:

1) The bodies are formed of linearly elastic materials and are homogeneous.
2) The contact area is essentially flat and small with respect to the typical dimensions of the bodies' geometries.
3) No sharp variations exist in the geometries of the bodies.
4) Inertial effects are small with respect to the contact stresses and may be ignored.

These assumptions allow for the usage of the influence function method [26, 27] (also known as half space approach). Due to the violations of the half-space assumptions, the conformal contact used to be a difficult problem to work out in CONTACT. With some FE-based adjustments on the influence function [31], the recent versions of CONTACT [32] have the option of solving the problems of conformal contact. The accuracy of CONTACT solutions has been verified/validated in [12, 26].

3.2 Integration CONTACT with FE model

Using CONTACT, a variety of contact problems, including the frictionless, frictional, stationary and non-stationary contact, can be addressed [27]. In order to perform the FE modelling verification against CONTACT, the CONTACT simulation has been integrated with the explicit FE analysis as shown in Figure 3. Such an integration is necessary to ensure that both models describe the same wheel-rail interaction process. It is worth noting that the primary focus of this study is extending the FE model verification from the Hertzian contact

problems, which have been successfully studied in [8, 9], into the common non-Hertzian contact problem due to the consideration of the realistic wheel-rail contact profiles.

Also, it should be mentioned that the proposed integration procedure is inspired a lot by the instructive analysing procedure of CONTACT [27] (i.e., the non-Hertzian contact analysis method) and the pioneering research progress made in [5, 8, 9, 16].

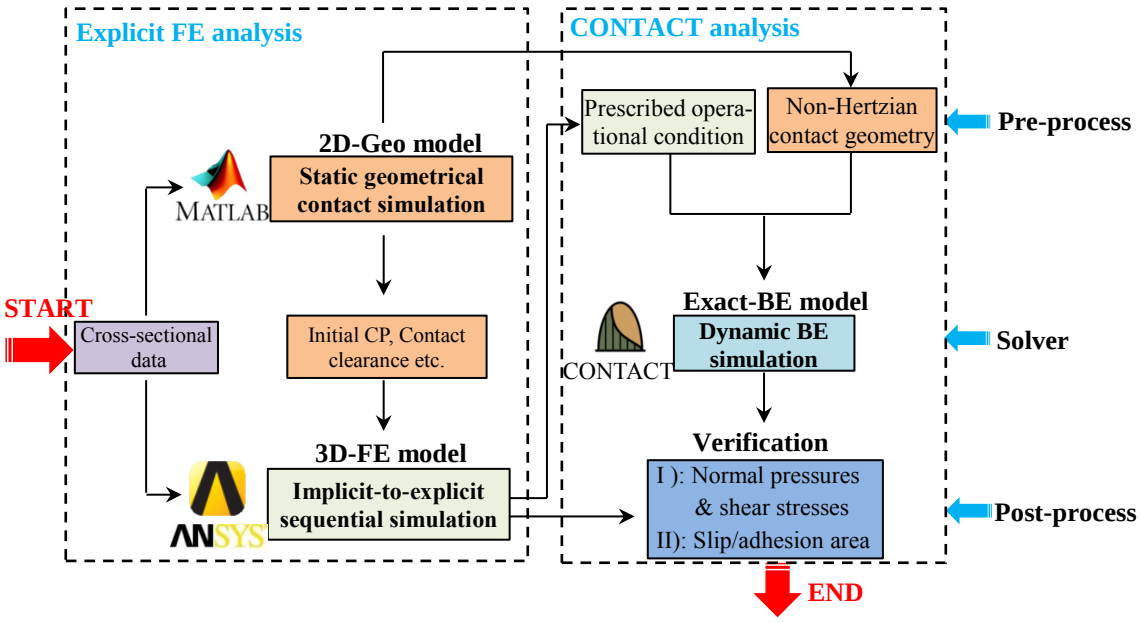

Figure 3. Integration procedure of CONTACT with FE model.

From Figure 3, it can be seen that there are three models involved in the verification process, namely, 2D-Geo model, 3D-FE model and Exact-BE model (CONTACT). Here, the abbreviation of "BE" refers to the "boundary element" method. The integration procedure consists of two parts, explicit FE analysis and CONTACT analysis. In the part of explicit FE analysis, the 2D-Geo contact analysis is performed first to determine the geometrical contact information such as the initial "just-in-contact" location (CP), the contact clearance and the corresponding local wheel rolling radius at the point of contact. The obtained contact information is used as the adaptive guidance for the mesh refining and dynamic loading application in the 3D-FE analysis. More information of the explicit FE analysis coupled with 2D-Geo contact analysis can be found in [22, 33, 34].

In the other part of the integration procedure, there are three major steps involved in the CONTACT analysis [27]:

1) Pre-process: setting up the contact geometries and applying the prescribed loads;
2) Solver: defining the analysis type/options and running the solving processor;
3) Post-process: reviewing the CONTACT results with the plot routines integrated;

As the solver of CONTACT is well-established, only limited items such as defining the analysis type/options are allowed to tune. For the Pre-process and Post-process, more preparations are needed for accurately performing the CONTACT analysis.

For instance, in the pre-process, the same input of the non-Hertzian contact geometries that

are defined in the coupled 2D geometrical contact analysis (a part of the FE model) is used in both models (FEM and CONTACT) (See Section 3.2.1). The operational conditions such as the contact loadings, train velocities, etc., in CONTACT are prescribed by the ones of the FE outputs (See Section 3.2.2). By this means, the consistency between the explicit FE analysis and CONTACT analysis can be guaranteed. Also, the correctness of the verification procedure can be assured.

In the post-process, the outputs of normal contact pressure, shear stress and slip/adhesion area, etc., exported from FE simulations are compared with the ones obtained from CONTACT analysis. In the following two sub-sections, the approaches of the Pre-process would be detailed. For the Post-process, it will be discussed in Section 3.3.

3.2.1 Non-Hertzian contact geometry

According to the integration procedure displayed in Figure 3, the non-Hertzian contact geometry has to be characterized first. The general operational steps [27] for such a characterization is demonstrated in Figure 4.

1) The calculation starts by defining the coordinate systems that are used. Figure 4a shows the un-deformed state of the contact geometry in the track-based coordinate system $O^t - X^t Y^t Z^t$, which has its origin at the track centre-line in the plane resting on top of the rails. Figure 4b presents a close-up view of wheel and rail profiles at the contact-based coordinate system in which Y-direction $O_c^{'} Y_c^{'}$ is normal to the contact plane. The origin $O_c^{'}$ is positioned in the initial contact point and the $Z_c^{'}$ axis is parallel to the Z^t-axis of the track-based coordinate system.
2) It is seen from Figure 4a that the calculation of the initial contact points on left and right wheels are accomplished based on the 2D-Geo contact model.
3) Rotating the wheel and rail profiles according to the resulting contact angle δ at the detected initial contact point O_c (See Figure 4b), the new wheel and rail profiles will be obtained in a tuned contact based coordinate system $O_c - X_c Y_c Z_c$.

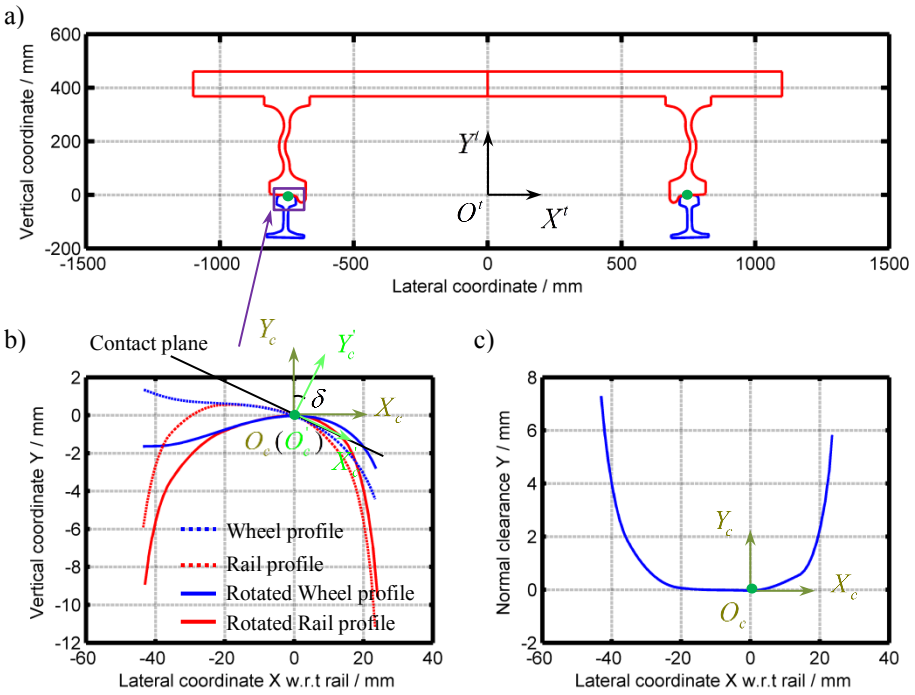

Figure 4. a). Wheel-rail contact geometry at track-based coordinates $O^t - X^t Y^t Z^t$; b). Close-up view of the wheel-rail profiles at two contact based local coordinate systems $O_c - X_c Y_c Z_c$ and $O_c^{'} - X_c^{'} Y_c^{'} Z_c^{'}$; c). The resulting normal clearance at lateral displacement $\delta x = 0mm$.(Notation: green solid circle refers to the initial contact point);

4) Interpolating the new rotated wheel and rail profiles with respect to a common set of lateral coordinates $\mathbf{X}$, and then assessing the un-deformed distance between wheel and rail profiles. Here, the un-deformed distance is referred to as the contact clearance $\boldsymbol{\delta y}$. The obtained contact clearance shown in Figure 4c is one required contact property for CONTACT. Using the obtained contact clearance, a potential contact area that encompass the real contact area could thus be identified and further used as an input for the CONTACT solving procedure.

It has to be mentioned that the integration of 2D-Geo model with CONTACT is seamlessly programmed. The wheel and rail contact geometries (solid lines as shown in Figure 4a and dash lines as shown in Figure 4b) have been substituted for the contact clearance curve to prescribe the potential contact area.

3.2.2 Prescribed operational conditions

To maintain the consistency between the FE simulations and CONTACT, the same elastic material properties, friction coefficients and the track geometries are used for both cases. They are shown in Table 1.

With respect to kinematic parameters, the prescribed total forces have to be specified according to the results obtained from the dynamic FE analysis (See Figure 5). The resulting force components in the Mid A_C area, which are extracted at the moment when the wheel passes through the middle of the solution area, are used as the prescribed loading conditions in CONTACT.

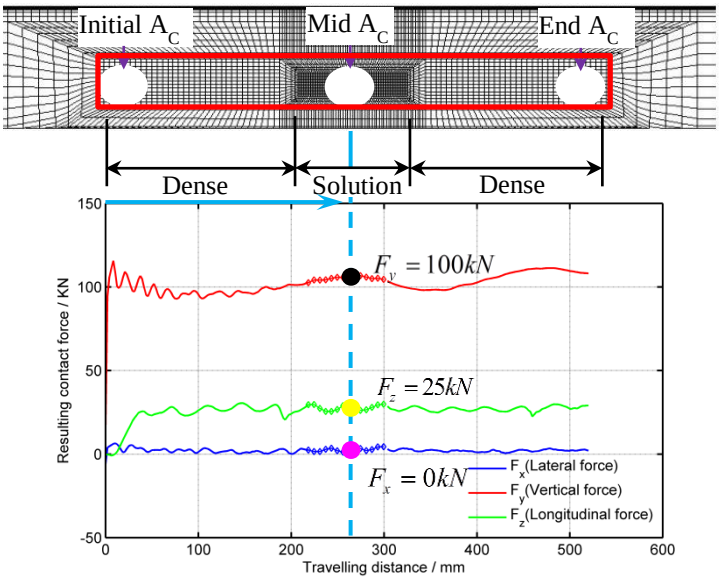

Figure 5. Resulting contact forces variation w.r.t rolling distance from FE analysis.

3.3 Verification results

Following the Post-process of the CONTACT analysis as demonstrated in Section 3.2, the FE results (such as the normal pressure, shear stress, the slip-stick area within the contact patch etc.) are compared with the ones obtained from the CONTACT simulations in this verification.

3.3.1 Normal pressure

As indicated by the method presented in [8], the contact patches from both the FE and CONTACT analyses are determined according to the normal contact pressure as follows:

$$\text{A node is in contact if: } |\sigma_n| > 0 \tag{5}$$

where σ_n is the nodal pressure in the direction normal to the local contact surface.

Figure 6a-b shows the normal pressure distribution calculated from the FE programme. In order to better demonstrate the resulting surface pressure distribution, the compressive normal pressure here is treated as positive. The results obtained from CONTACT are shown in Figure 6c-d. All the resulting contact patches are non-elliptical. The reason of the non-elliptical contact patch can be attributed to the changing radius of the curvature of the realistic wheel/rail local contact geometries as well as to the rail inclination angle (1/40) considered in the model.

Also, it is observed that these contact areas are shorter in the rolling direction than the length in the lateral direction. In addition, the contact patches are approximately symmetrical with respect to the vertical-lateral plane. The peak of the contact pressure is located at the vicinity of the initial contact point. The distribution of the contact pressure has a similar pattern, i.e., the higher contact pressure is positioned at a region that is much closer to the side of gauge corner (G.C.) than to the field side (F.S).

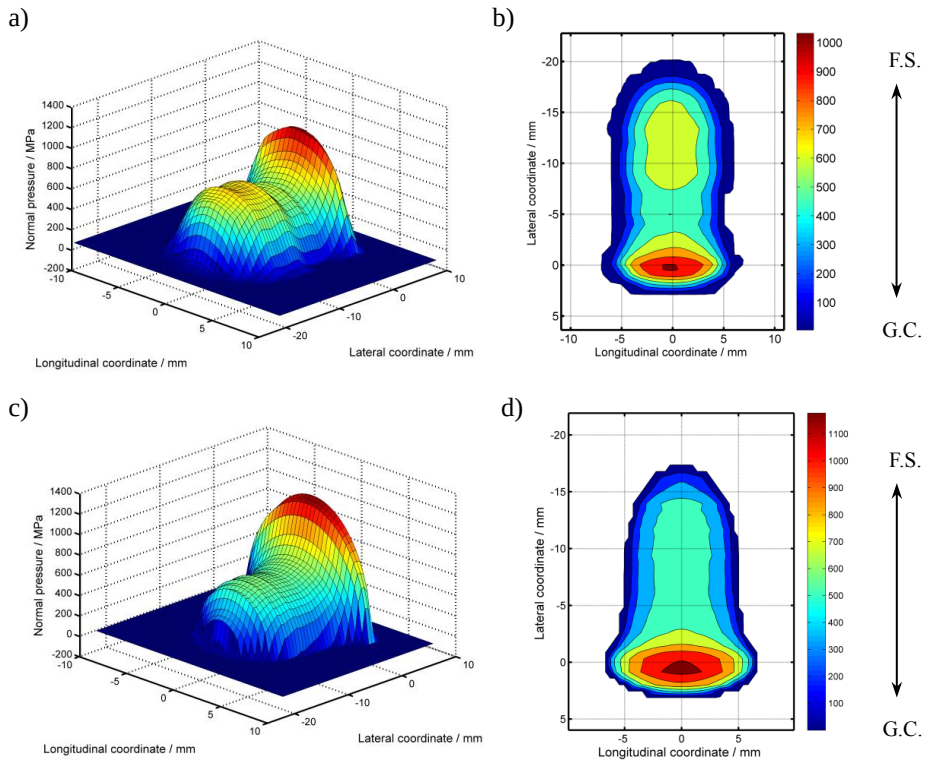

Figure 6. Normal pressure distribution. a) FE surface plot; b) FE contour plot; c) CONTACT surface plot; d) CONTACT contour plot. (Note: G.C. means the gauge corner, F.S. means the field side).

Table 2 lists the quantitative results in terms of the maximum normal pressure and the contact patches. The maximum length of the contact patch in lateral direction is 22.91mm in the FE solution, whereas in CONTACT it is 20.48mm. That has resulted in the relative difference between the area of the contact patch in both solutions of 28.23% as it can be seen from Table 2 ($256.5mm^2$ in the FE solution and $200.02mm^2$ in the CONTACT solution). Besides, the maximum normal contact pressure, which amounts to 1226MPa, is obtained in CONTACT that is 13.95% higher than the FE solution.

Table 2. Comparison of the normal solutions of the two approaches.

Approach	Maximum normal pressure	CONTACT patch		
	σ_{max} / *MPa*	Maximum length in lateral direction / mm	Maximum length in longitudinal direction / mm	Area / mm^2
CONTACT	1226	20.48	13.33	200.02
FE	1055	22.91	14.08	256.5
Difference w.r.t. CONTACT	-13.95%	11.87%	5.63%	28.23%

It can be seen that although the percentage deviations of contact pressure exist, the FE results agree reasonably well with the ones from CONTACT simulations. The sources of these discrepancies can be categorised into three groups, namely, the different analysis types, the FE penalty approximation and the tangent contact planes.

1) Analysis types: CONTACT uses a quasi-static approach [27], while the FE analysis type is transient. It can be observed from the FE simulation results (See Figure 5) that both the vertical and longitudinal forces are varying with respect to travelling distances. Since these varying resultant contact forces are composed of the nodal

resistive contact pressures/stresses, the transient behaviour of the explicit FE analysis would manifest itself in the discrepancies of the normal contact pressure and the actual contact patch shown in Table 2.

2) Penalty approximation: It is known that penalty method (See Section 2) is used to satisfy the contact conditions approximately [35, 36] in the explicit FE analysis.. Moreover, the penalty method can also affect the stability of the explicit time integration procedure, since the central difference method is conditionally stable [37]. In the penalty method, the choice of the interfacial parameters (contact stiffness, damping, etc.) should be made depending on the particular problems considered in order to obtain the accurate results. Therefore, the study on the influence of the wheel-rail interfacial parameters on the contact stability and accuracy of the results had been done by the authors recently [38]. In this paper, the optimal set of the interface parameters as proposed in [38] has been used. But still, this approximate contact constraint enforcement may influence the FE results and ultimately cause the discrepancies between FE and CONTACT solutions.

3) Tangent contact planes: It can be seen from Section 3.2.1 that the potential contact area in CONTACT is prescribed on the basis of the contact clearance, which is determined by the local tangent contact planes (involving the parameters such as the initial contact point, contact angle, etc.) obtained from the home-made 2D-Geo contact simulation. These tangent contact planes are calculated under the static, un-deformed state, which would be different from the ones at the dynamic, deformed state in reality. Also, the choice of the inputted resulting contact clearance curve would influence the actual contact patch and the pressure distribution obtained using the CONTACT programme.

   The detection of the potential contact area in the FE analysis is much different. Two large enough potential master and salve contact segments are prescribed respectively (See Figure 1g-h). As it has been discussed in Section 2, the contact forces are predicted iteratively using central difference method. No local tangent contact planes are needed to be predefined in the FE simulation.

3.3.2 Surface shear stress

Figure 7a-b shows the surface shear stress distribution calculated from FE programme, while Figure 7c-d presents the one obtained from CONTACT programme.

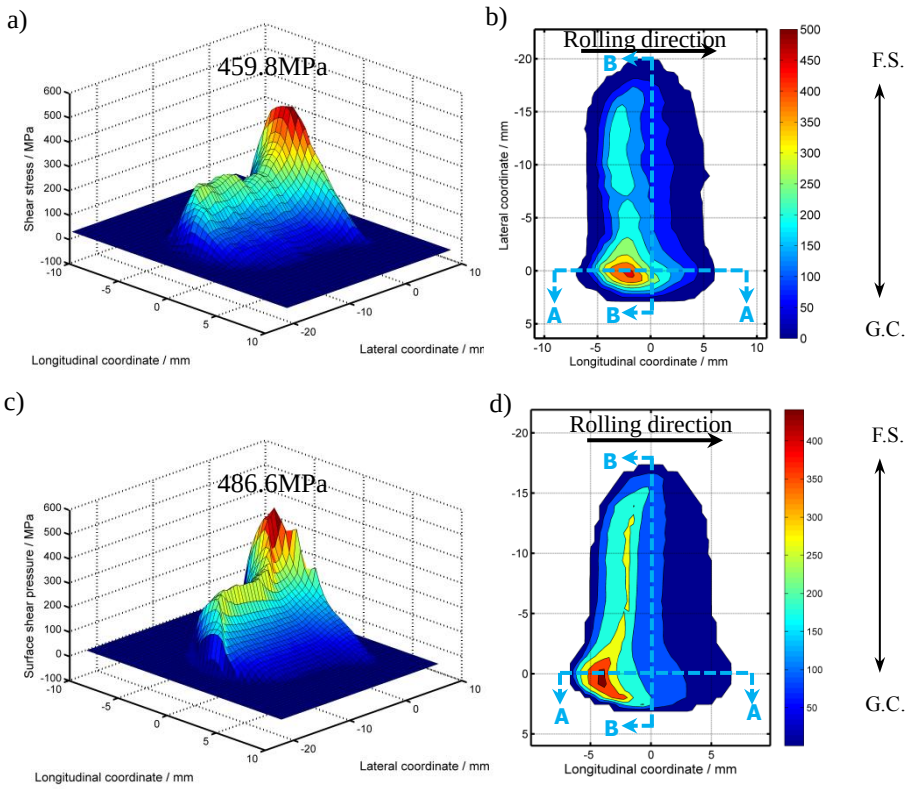

Figure 7. Surface shear stress distribution. a) FE surface plot; b) FE contour plot; c) CONTACT surface plot; d) CONTACT contour plot. (Notation: blue dash lines refer to the cutting planes, namely AA and BB).

It can be seen that the shear stress distribution of the FE solution is comparable with the one of CONTACT solution. The major portion of the shear stress is located at the rear part of the contact patch. The maximum surface shear stress of FE solution and CONTACT solution amount to 459.8MPa and 486.6MPa respectively.

In order to create a cross-sectional view of the 3D surface shear stress, two orthogonal sliced planes, namely "AA" and "BB", are introduced as shown in Figure 7b & 6d. "AA" is sliced at the initial contact point along a longitudinal-vertical plane, while "BB" is cut at the same point but along a lateral-vertical plane.

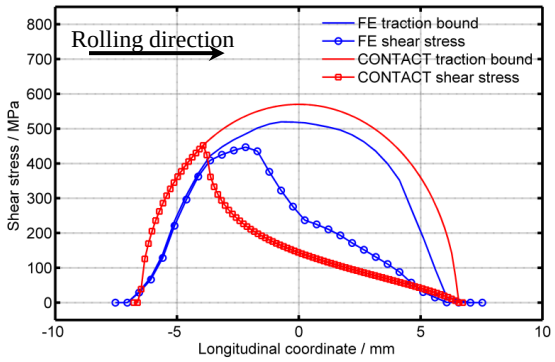

Figure 8. 2D surface shear stress slice plot.

Figure 8 displays 2D surface shear stress sliced at the "AA" plane. It is observed that the shear stress is limited by a traction bound (denoted by solid red and blue curves), which is the product of the normal pressure and the friction coefficient μ. Thus, the difference between

the normal pressure as shown in Figure 6 also manifests itself in the discrepancies between traction bounds as well as the shear stresses obtained from FE and CONTACT analysis.

It is also observed that the shear stress curves from CONTACT are much smoother and more disciplined than the ones obtained from FE simulations. Such a phenomenon could be explained by the difference of the contact solving procedures between CONTACT and FEM. In CONTACT [26], the normal and tangential friction problems are solved sequentially. The tangential traction are to be calculated until the normal pressure is known.

For the case of explicit FE analysis, Coulomb formulation [23, 24] is used to predict the tangential frictional force. The normal and tangential problems are calculated simultaneously for all the cases of contact problems. Using the central difference method [1, 24, 37], all the nodal forces including both the tangential and normal ones are calculated iteratively from the present time step to the next one.

3.3.3 Slip-adhesion

Based on the calculated normal pressure and surface shear stress, the slip-adhesion phenomenon can be further explored using the following equation adapted from [8]:

$$\text{The node is in adhesion if: } \mu\left|f_{n\_N}\right| - \left|f_{n\_T}\right| > \varepsilon_T \tag{6}$$

where f_{n_N} is the nodal normal force, f_{n_T} is the nodal tangential force in the longitudinal direction, and ε_T is the tolerance for distinguishing the slip and stick areas. The magnitude of ε_T is prescribed to be the 10% of the maximum traction bound force $(\mu\left|f_{n\_N}\right|)$.

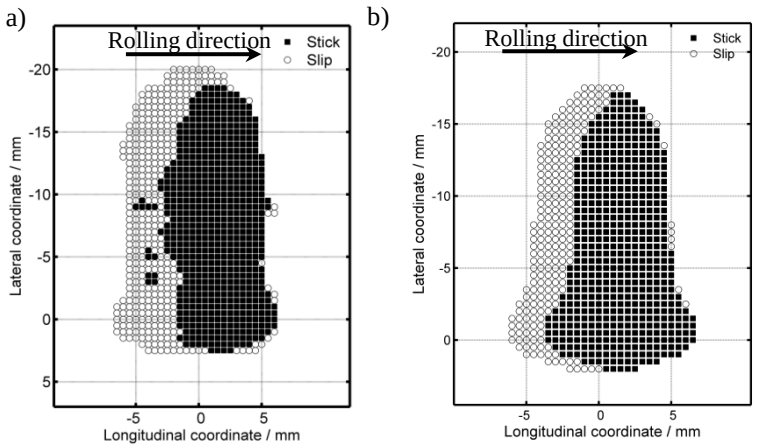

Figure 9. Slip-stick area plot. a) FE result; b) CONTACT result.

It has to be mentioned that the tolerance used here is not as rigorous as the one in [8], since the present tolerance is applied on the contact patches resulting from the realistic wheel/rail contact geometries.

Figure 9a-b shows the slip-stick area distributions in the contact patches based on the criteria stated in Equation (6). As it can be observed, the leading edge of all the contact patches is in stick, whereas the trailing edge is in slip. Such an observation conforms well with the classical rolling contact theory [26]. In addition, it can be seen from the FE result (Figure 9a) that some of the "stick" grids seems to be misplaced inside the "slip" zone, while the CONTACT result

(Figure 9b) tends to be much disciplined and ordered.

From Equation (6), it is observed that the slip-stick area is strongly dependent on the relationship between normal pressure and shear stress. The tolerable differences of normal pressure and shear stress have been explained in the previous two sub-sections. Also, the tolerance ε_T for identifying slip-stick area is much larger than the one in CONTACT (zero tolerance). Thus, it is reasonable to see the difference in the slip-stick areas obtained from CONTACT and FE analysis.

From the results and discussions, it can be noticed that the developed FE model is able to simulate the wheel-rail interaction effectively. The obtained FE results are comparable with the ones of CONTACT. The discrepancy between the results of CONTACT and FEM simulations is reasonable enough for the developed FE model to be used in the future research. However, as one major disadvantage of the FE analysis, it has to be mentioned that the computational expenses of the FE simulation (around 9 hours) are much higher than the ones of CONTACT simulation (2~3 minutes).

4 Parametric study

The knowledge on the influence of operation patterns on the tribological behaviour of wheel and rail interaction is always in high demand for formulating the appropriate operational strategies (increasing/decreasing friction/traction, etc.) to improve the performance of railway system. To enhance such knowledge, the following parameters are varied to conduct the parametric study starting from the reference case (See Table 1):

1) the friction coefficient (changing from 0.0 to 0.8);
2) the traction forces (varying from braking to accelerating);
3) the lateral position of the wheel (shifting from -5.5mm to 5.5mm);
4) the material properties, by varying the yield strength limit from 280MPa to 680MPa.

The corresponding results and discussions are presented below.

4.1 Friction coefficient

To study the resulting stress states and contact properties under different frictional levels, nine sets of FE simulations have been performed with the friction coefficient ranging from 0.0 to 0.8. In Figure 10, the dynamic response of the resulting longitudinal friction forces with different friction coefficients are presented. From this figure, it can be seen that the change of friction coefficient can bring about a dramatic influence on the variation of the longitudinal force.

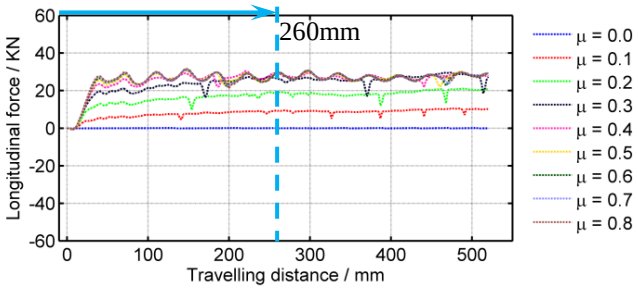

Figure 10. Resulting longitudinal friction forces from the variation of friction coefficient. (Note: the intersecting point between the blue dashed line and the curves of the longitudinal forces indicates the position in which the contact properties are extracted.)

At zero friction coefficient, no longitudinal forces are observed. When the friction coefficient is increased, the resulting contact patches start to transfer the traction for the wheel to accelerate. For the cases of friction coefficient varying from 0.1 to 0.3, the stair-type growth trend of longitudinal force is observed. With the friction coefficient increasing steadily over 0.3, the longitudinal friction forces reach to its saturated value 25kN and remain the same. This phenomenon is due to the fact that the applied traction is determined (traction coefficient $T = 0.25$) for all the cases of varying friction coefficient. As a result, the higher the friction coefficient is, the larger the longitudinal friction force within a upper bound of 25kN occurs.

It can also be seen that all the resulted longitudinal friction forces are varying with respect to the travelling distance. These variations are getting more noticeable at high friction levels than the ones at low friction levels, even the studied wheel and rail interfaces are flat and have no defect. It is observed that the oscillation of the longitudinal friction force is highly related to the magnitude of κ, which is the ratio of the traction coefficient T to the friction coefficient μ. The smaller the magnitude of κ is, the more noticeable the oscillations of the frictional forces are. Also, κ is an index to assess the contact status:

$$\text{The contact is in partial slip if : } \kappa < 1 \tag{7}$$

Thus, the noticeable oscillations at high friction levels means that the corresponding contact statuses are partial slip. In other words, the friction forces in partial slip tend to introduce more oscillations than the ones in full slip.

Figure 11 shows the influence of the oscillatory longitudinal forces on the shear stress distributions at the friction coefficient μ of 0.8. Four time moments ranging from A to D are selected from the curve of the oscillatory longitudinal force. The corresponding shear stress distributions at selected moments are shown in Figure 11b. It can be seen that the local minimum longitudinal force located at “A” is approximately 24kN, whereas at “D” the local maximum longitudinal force amounts to 30kN. This has resulted in the relative difference of approximately 25% between the maximum shear stresses in both “A” and “D”.

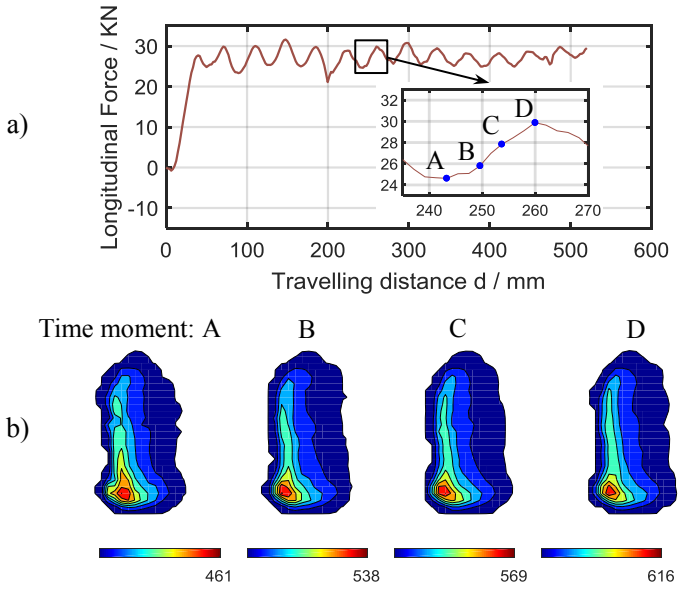

Figure 11. Effect of the oscillatory longitudinal force on the shear stress distribution. a) Longitudinal friction force at high friction level of $\mu = 0.8$; b) The corresponding shear stress (Unit: MPa) variation at specified time moment.

As the CONTACT calculations are made for the same time moment as FEM, the magnitudes of the resulting longitudinal forces obtained from FE simulations are used as an input in the CONTACT analysis. This makes the operational/loading conditions to be consistent for both CONTACT and FEM simulations. Therefore, the influence of the oscillatory variation of the longitudinal force on the lateral verification process would be insignificant.

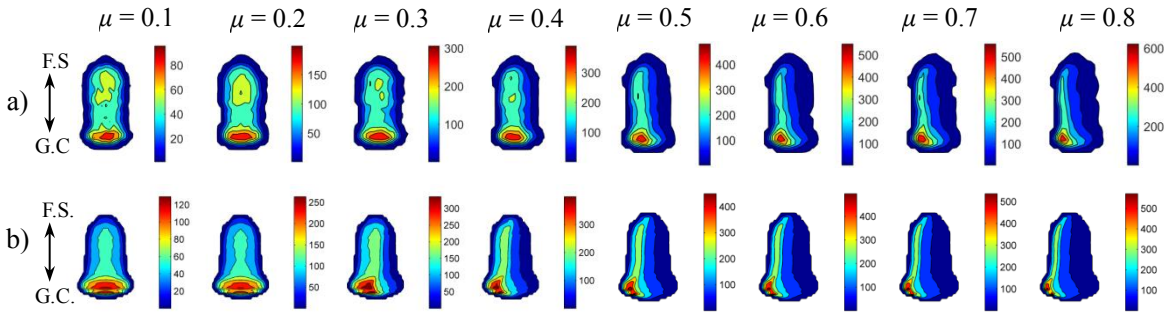

Figure 12. Shear stress distribution (Unit: MPa). a) FE solution; b) CONTACT solution.

The distributions of the surface shear stress are shown in Figure 12. These contact properties are extracted at a distance of 260mm from the starting point (See Figure 10). It can be further seen that both the FE solution (Figure 12a) and the CONTACT solution (Figure 12b) demonstrate the gradual change of the surface shear stress as the friction coefficient is changing. Figure 13 shows the slice plot of the surface shear stress sliced at the initial contact point along the longitudinal direction. It is observed that the shear stress responses of both FE and CONTACT results exhibit the similar pattern.

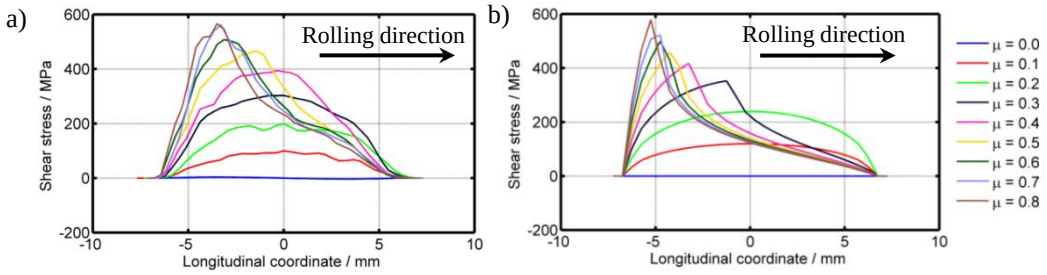

Figure 13. 2D Shear stress sliced plot. a) FE solution. b) CONTACT solution.

Figure 14 presents the slip-adhesion area variation for the different friction coefficients. It can be noticed that when the friction coefficient is lower than 0.3, saturation is reached in which full slip condition covers almost the whole contact patch.

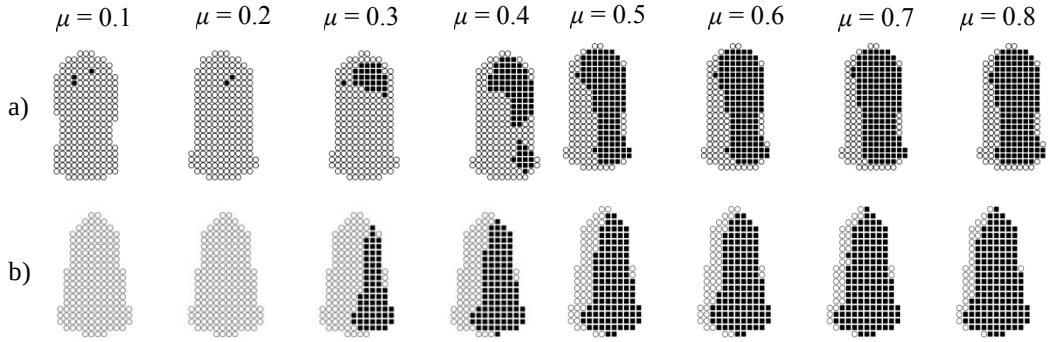

Figure 14. Slip-adhesion plot. a) FE solution; b) CONTACT solution. (Note: ○ refers to slip, ■ denotes stick).

With the increase of friction coefficient from 0.3 to 0.8, the slip area is getting smaller and smaller in comparison with the stick area. The slip-adhesion areas obtained from FE solutions agree well with the ones from the CONTACT solutions.

Using the "AA" cutting plane as demonstrated in Figure 7, the variation of the subsurface stress response is presented. It is clearly seen from Figure 15a that the maximum Von-Mises stress is shifting from sub-surface to surface with the increase of the friction coefficients, while for the shear stress distribution shown in Figure 15b, the tensile stress moves upward as well.

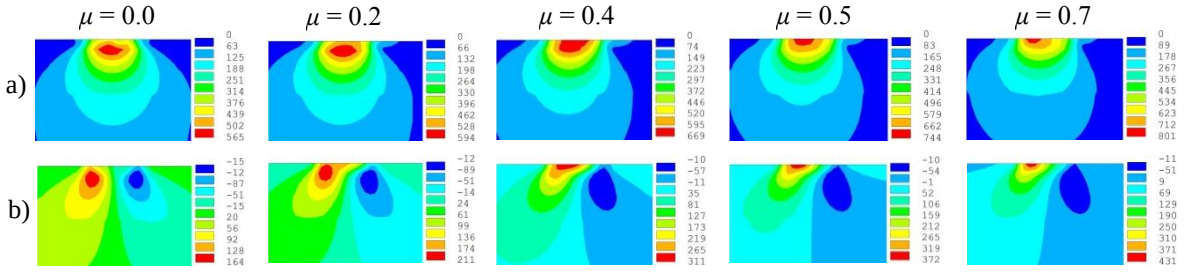

Figure 15. Sub-surface stress distribution (Unit: MPa). a) Von Mises stress; b) Shear stress.

The results correlate quite well with the surface shear stress distribution shown in Figure 12, in which the higher friction coefficient will lead to smaller slip area and higher surface pressure causing that the higher shear and Von-Mises Stress (VMS) shift upward to the surface. It has been confirmed by the research from [39] that when the friction coefficient is larger than 0.45, surface damage such as head check is getting dominant.

4.2 Traction forces

When the vehicle travels along the track, three typical operational conditions can occur, namely accelerating, free rolling and braking, which are schematically shown in Figure 16. For the case of free rolling, no traction forces will be applied and the translational velocity is proportional to the angular velocity, while for the braking and accelerating operations the direction of the driving torques are in opposite.

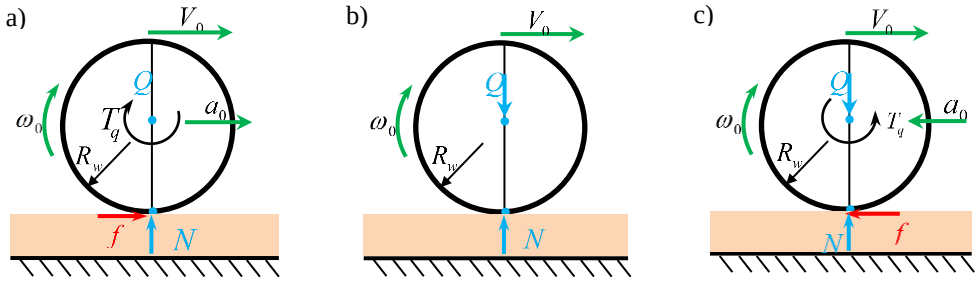

Figure 16. Schematic graph of train operations. a) accelerating; b) free rolling; c) braking.

In order to study the influence of the train operations on the contact properties, a series of FE simulations has been performed. The corresponding results and interpretations would be reported in this section.

Figure 17 depicts the variation of the resulting longitudinal contact forces with different traction forces ranging from -50kN to 50kN. As it can be seen that, with the change of the operational conditions from accelerating to braking, the resulting longitudinal force starts to alternate its direction from positive to negative. The stair-type growth trend of traction forces is getting even more pronounced than the cases shown in Figure 10, when the traction coefficient T is increasing from -0.5 (braking) to 0.5 (accelerating).

It can also been seen that the force oscillations are being greatest at the medium traction force transmission levels. As the ratio $|\kappa|$ of traction coefficient $(T=-0.5\sim 0.5)$ to friction coefficient $(\mu=0.5)$ is smaller than 1 at medium traction force transmission levels $(|T|=0.25)$, the corresponding contact status is partial slip. As a result, there are more force oscillations observed.

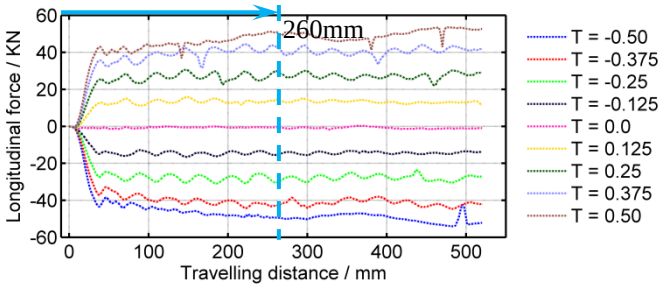

Figure 17. Resulting longitudinal contact forces from the variation of traction forces. (Note: the intersecting point between the blue dashed line and the curves of the longitudinal forces indicates the position in which the contact properties are extracted.)

Figure 18a-b shows the distribution of the resulting surface shear stress. For the CONTACT solutions, when they are compared between the braking and accelerating operations with the same traction amplitude, the shear stresses exhibit the same amplitudes but opposite signs.

Also, it can be seen that the "focusing point" of the shear stress is always located at the side close to the gauge corner (G.C.). Here, the "focusing point" defined as the most stressed point.

Regarding the case of the FE solutions as shown in Figure 18a, the "focusing point" of the shear stress is much concentrated on the field side (F.S.) when the wheels are at braking ($T = -0.125 \sim -0.25$), while the accelerating operation ($T = 0.125 \sim 0.25$) pushes the "focusing point" of the shear stress towards the side of the gauge corner (G.C.). Generally, the magnitude of the shear stress from FE solution is lower than the one from CONTACT solution.

Such a movement of "focusing point" observed from FE results could be caused by the special "conical" wheel contact geometry. As a result, the resulting tangent contact plane has a inclined angle with the horizontal plane. This inclined tangent contact plane would lead to the local wheel rolling radius difference between the two areas of field side and gauge corner. When the wheel rolls over the rail under accelerating operations, the large local wheel rolling radius would bring much local slip to the side of the gauge corner. Yet, the small local wheel rolling radius would generate much local slip to the side of the field side under braking operations.

As it has been discussed in Section 3.2.1 and Section 3.3.1, the tangent contact planes are determined by the 2D-Geo contact analysis. Also, the choice of these tangent contact planes may influence the imported contact clearance curve (non-Hertzian contact geometry) and ultimately the CONTACT solution. To minimise such an influence, more research efforts are required to improve the functionality of the present 2D-Geo contact model. By this means, the change of the local wheel rolling radius resulting the movement of the "focusing point" is able to be considered in the improved 2D-Geo contact model. This explains the difference of the CONACT and FE simulations results under accelerating and braking operations.

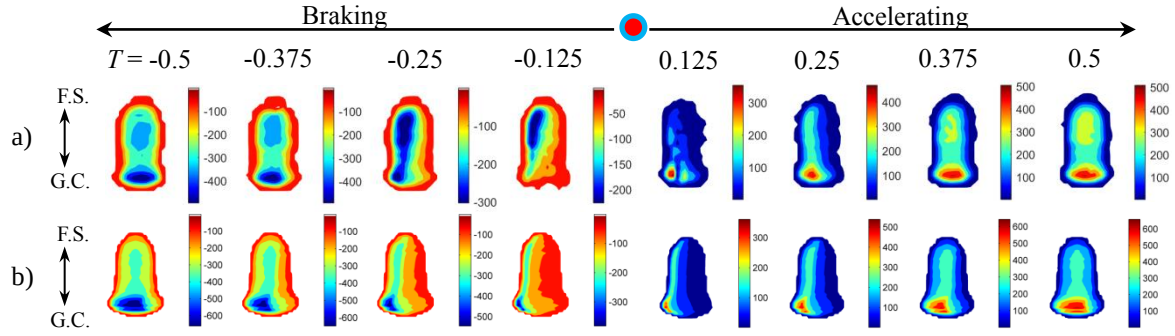

Figure 18. Surface shear stress distribution (Unit: MPa). a) FE solution; b) CONTACT solution.

Figure 19 shows the 2D slice plots of the surface shear stress distribution at "AA" cutting plane. The shear stress is almost equal to zero under free rolling, while for the accelerating and braking operations, the shear stresses exhibit completely opposite behaviour, which further confirmed the afore observations. Also, a large spike is observed at the traction coefficient of 0.125. This spike also manifest itself in the discontinuities of the corresponding contour plot as shown in Figure 18a ($T = 0.125$). Since the traction force is very small, the shear stresses are distributed at a rather narrow strip. The insufficient mesh grids within the strip may cause the spike oscillation. In the simulation with refined mesh, the spike has been

considerably reduced.

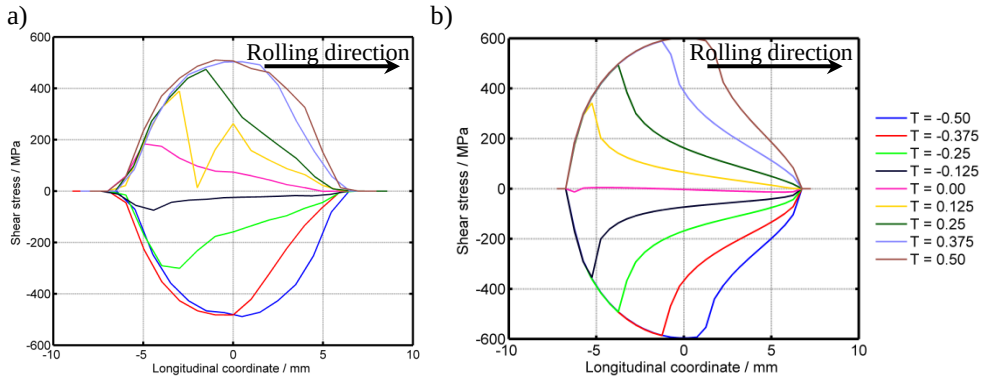

Figure 19. 2D surface shear stress sliced plot. a) FE solution; b) CONTACT solution.

According to the shear stress distribution presented above, the distribution of the slip-adhesion areas are presented in Figure 20a-b. It is apparent from Figure 20a that much slips obtained from FE solutions are shifted to field side for braking operation and to gauge corner for accelerating, respectively. The "focusing point" movement of the shear stress as shown in Figure 18 also manifests itself in the slip-stick are distribution. The pattern of the slip-adhesion distribution obtained from the FE solutions agrees relatively well with the ones from CONTACT solutions.

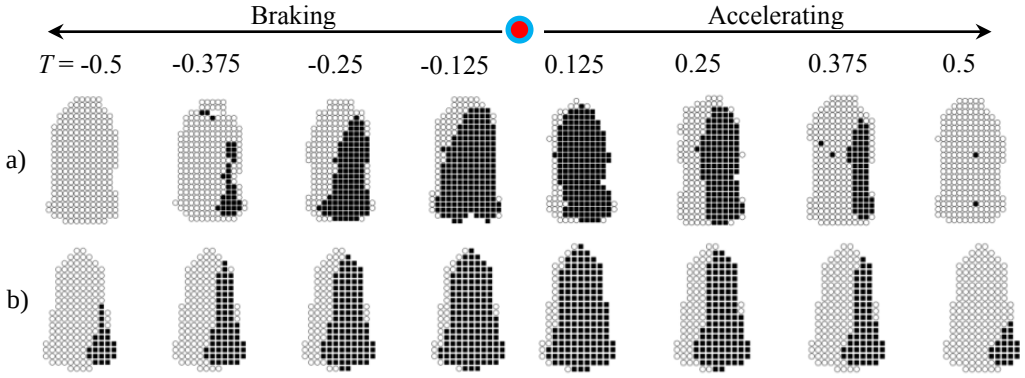

Figure 20. Slip-adhesion plot. a) FE solution. b) CONTACT solution. (Note: ○ refers to slip, ■ refers to stick)

Figure 21 shows the sliced plots of the sub-surface stress responses under three typical operational conditions at the "A-A" cutting plane. In the free rolling processes, the shear stresses are distributed almost symmetrically to a distinguishable axis. In the accelerating process, the VMS stress distribution on the surface was extended to the right – (in front of the wheel) the positive shear stress was dominant on the top rail surface. For the braking operation, the VMS stress distribution on the surface was stretched to the left (behind the wheel) and the negative shear stress was dominant on the top rail surface.

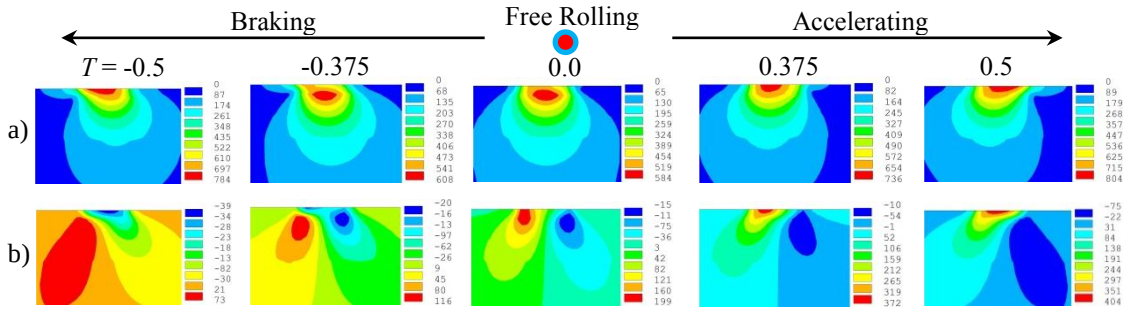

Figure 21. Sub-surface stress distribution in AA-plane (Unit: MPa). a).Von Mises stress; b). Shear stress;

It is obvious that the solutions of the contact properties obtained from these two approaches are relatively well in accordance with each other, in spite of the occurrence of the deviations, such as the change of "focusing point", the variation of the shear stress amplitudes, etc. From the parametric studies on traction forces, it can be concluded that the developed FE tool can produce as good results as CONTACT.

4.3 Contact point

The contact point distribution under different wheelset lateral shifts was determined using the 2D-Geo model. As it can be seen from Figure 22 the refined mesh region is automatically adjusted according to the location of the contact point. Based on the developed FE models, the influence of the contact point variation due to the various lateral shifts of the wheel set (-5.5, -3.5, -2, -1, 0, 1, 2, 3.5, 5.5mm) on the wheel-rail contact behaviour is analysed in this section.

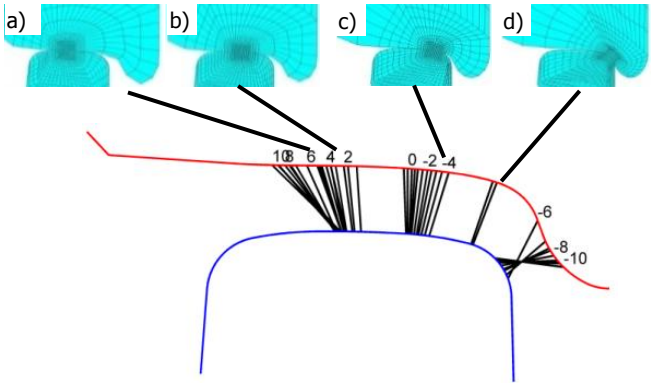

Figure 22. Contact points distribution. a) 5.5mm; b) 2.0mm; c) -3.5mm; d) -5.5mm.

Figure 23 shows the two solutions of the contact area evolvement as the wheel is displaced over the rail with different lateral shifts. It can be seen that the non-elliptical contact patches prevail again. The reason of that is attributed to the fact that the radii of the curvature of both wheel and rail change significantly within the area of contact. Moreover, it is observed from FE solution (Figure 23a) that the magnitudes of the maximum normal pressure are on a steady decline from the lateral displacement of -5.5mm (2311MPa) to 0.0mm (1518MPa), while they switch into another trend of slight increase for the rest cases varying from 1.0mm (856MPa) to 5.5mm (1191MPa). From Figure 23b, it can also be seen that the trends of the CONTACT solution are quite similar to that of the FE solution. Regarding the magnitude of the normal pressure, the CONTACT results seem to have a higher value than the FE results in most cases.

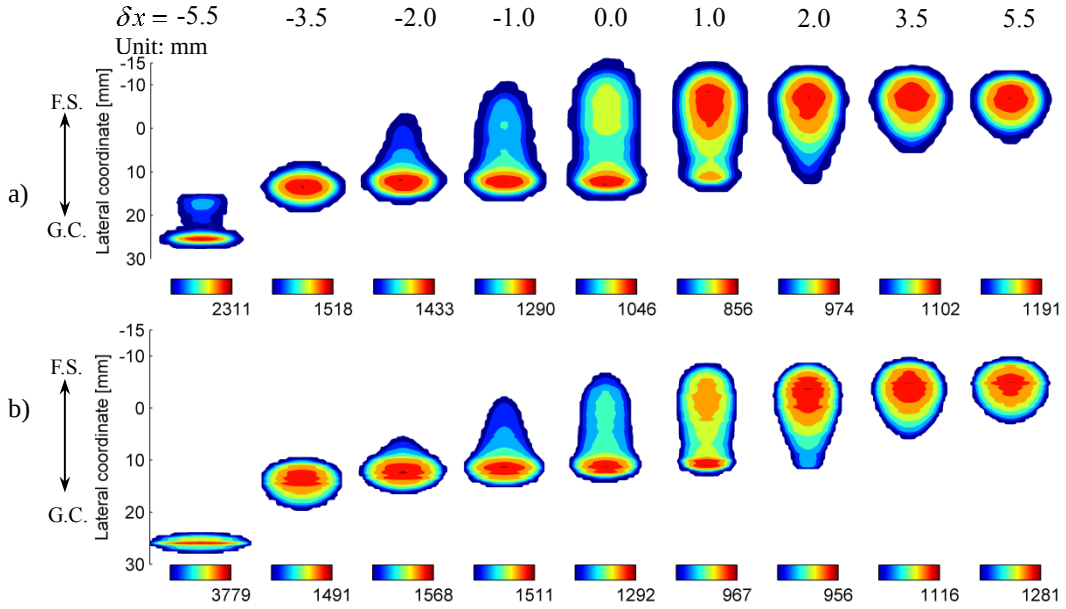

Figure 23. Normal pressure distribution (Unit: MPa). a) FE solution; b) CONTACT solution.

For the lateral shift of -5.5mm, contact between the wheel flange root and rail gauge corner occurs (See Figure 22d), there is a drastic difference in terms of the resulting contact area as well as the magnitude of the normal pressure between the two solutions. It can be interpreted by the fact that the wheel and rail contact geometries are getting much curved and non-planar in this case. Thus, the identification of the potential contact area (i.e., the contact clearance curve) and the accurate tangent contact plane using the 2D-Geo contact model would be influenced. As it has been mentioned in Section 4.2, more research efforts are required to improve the functionality of the 2D-Geo contact model so as to minimise the negative influence that it brings to the CONTACT solution.

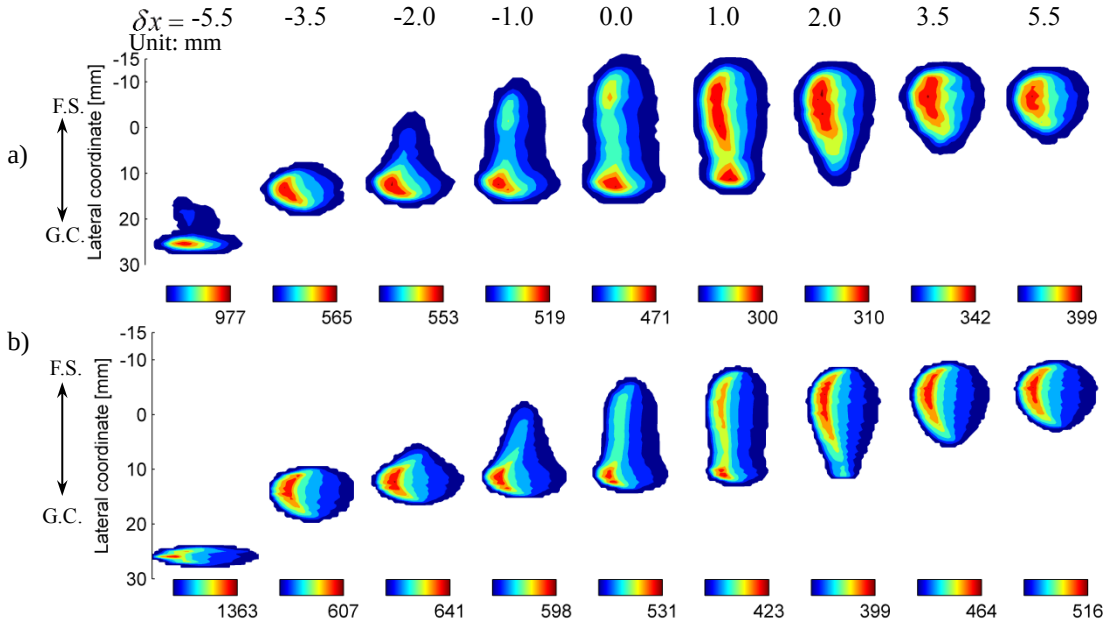

Figure 24. Shear stress distribution (Unit: MPa). a) FE solution; b) CONTACT solution.

Figure 24 shows the two solutions of the associated surface shear stress at different lateral displacements. As the traction force is fixed, the distribution of the shear stress is directly

linked with the distribution of normal pressure as illustrated in Figure 23. Similar contact patches as well as discrepancies of magnitude have been observed from the two compared solutions.

Figure 25 shows the quiver plot of the surface shear stress at the lateral shift of -5.5mm, in which the large shear stress components towards to the lateral direction is observed. The reason is that the angle between the contact plane and the horizontal plane in the contact point is large enough to introduce a large lateral force, and such a lateral force component starts to play a much important role in the wheel-rail interaction. The green boxes indicate the boundary of the actual contact area obtained from the two approaches.

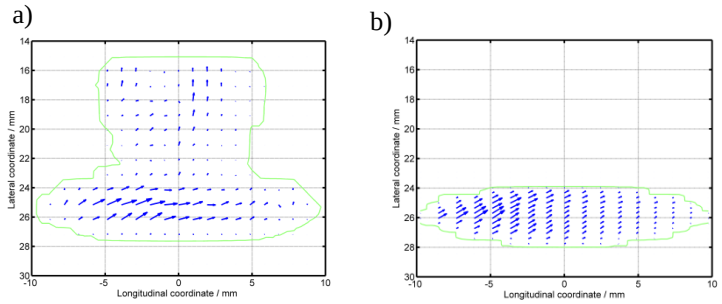

Figure 25. Surface shear stress quiver plot at the lateral shift of -5.5mm. a). FE solution; b) CONTACT solution.

Furthermore, the distribution of the subsurface VMS stress and shear stress along the "BB" cutting planes for the lateral shifts of 5.5, 2.0, 0.0, -2.0, -5.5mm are presented in Figure 26. If the stress distribution of the lateral shift 0.0mm was used as a reference, it can be noticed that the maximum shear and VMS stresses are shifting from field side to the gauge corner with the decrease of δx from 5.5mm to -5.5mm. When the contact occurs at the region of the gauge corner (-5.5mm), both the magnitude of the VMS stress and the shear stress exhibit a substantial increase of 1653MPa and 393MPa, respectively. Such a highly-stressed subsurface cross-sectional observation from the FE simulations also indicates a good agreement with the field observations, which states that the high contact stresses at gauge corner make main contribution for the initiation of the rail defects called head checks.

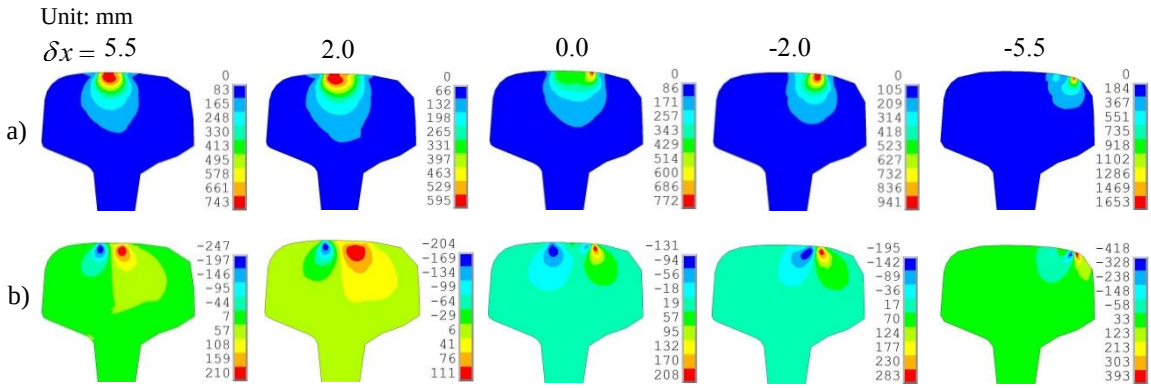

Figure 26. Sub-surface stress distribution of FE solution in BB-plane (Unit: MPa). a).Von Mises stress; b). Shear stress;

It can be further seen that both the surface and the subsurface stress responses, namely the distributions and magnitudes, are drastically influenced with the change of the contact points. These FE results can be used as a good basis for studying and interpreting the phenomenon of the crack initiation or propagation at different contact points. It can be concluded that the

developed FE tool is flexible, effective and reliable enough to simulate the cases of the contact point shifts.

4.4 Material properties

Four sets of numerical simulations have been carried out to study the effect of material properties on the resulting contact properties. One set of simulations consists of the elastic wheel-rail material with the Young modulus E and Poisson ratio ν kept constant at 210GPa and 0.3, respectively.

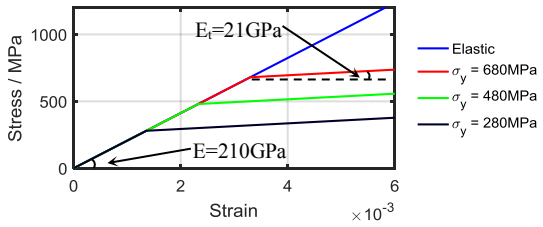

Figure 27. Schematic graph of the resulting bilinear elastic-plastic material model from the varying yield strength σ_y .

The other three sets consist of varying the material properties from the pure elastic to elastic-to-plastic ones. The yield strength σ_y for the elastic-to-plastic material is varying from 280MPa to 680MPa, whereas all the tangent modulus E_t is 21GPa. Here, Young modulus E represents the ratio of stress versus strain (slope) in the elastic range (See Figure 27). The Tangent modulus E_t refers to the slope of the stress-strain curve in the plastic range, which quantifies the "softening" of material that occurs when it begins to yield. The yield strength σ_y denotes the turning point in the stress-strain curve at which the stress-strain curve levels off and plastic deformation starts to occur.

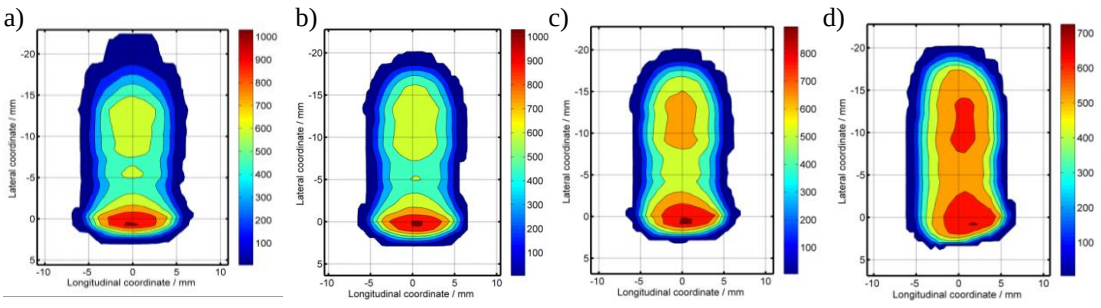

Figure 28. Normal pressure variation (Unit: MPa). a) infinite; b) 680MPa; c) 480MPa; d) 280MPa.

From the contour plots displayed in Figure 28a-d, it is observed that the pattern of the contact patch is changing from symmetry to non-symmetry. Due to the redistribution of stresses over a larger contact area obviously when using plastic materials in the case of the 280MPa yield strength, the magnitude of the maximum normal pressure (720MPa) is reduced up to 31.8% compared with the elastic materials (1056MPa).

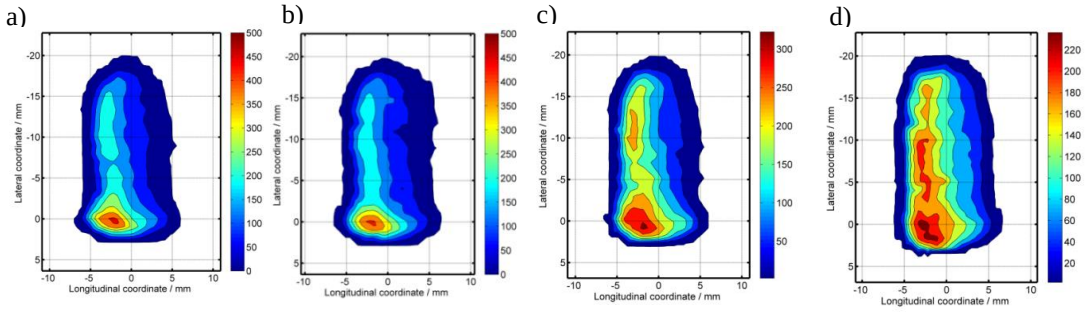

Figure 29. Surface shear stress distribution (Unit: MPa). a) infinite; b) 680MPa. c) 480MPa; d) 280MPa.

The surface shear stresses, which are transferring the traction forces over the contact areas, are shown in the Figure 29. Also, it can be seen that the maximum shear stress obtained from simulations with elastic-to-plastic materials in the case of the 280MPa yield strength (500MPa) was 55% lower in comparison with the elastic case (225MPa).

Figure 30 shows the residual VMS stress distribution along the path the wheel runs. For the material with high yield strength (See Figure 30a-b), there is no residual stress observed. However, when there were a lower yield strength limit adopted in the material model such as the cases shown in Figure 30c-d, a noticeable band highlighted with relatively high residual stress was observed. It can be observed that the remained running band is increasing from three or four millimetres in the case of the 480MPa yield strength to more than twenty millimetres with a yield strength of 280MPa.

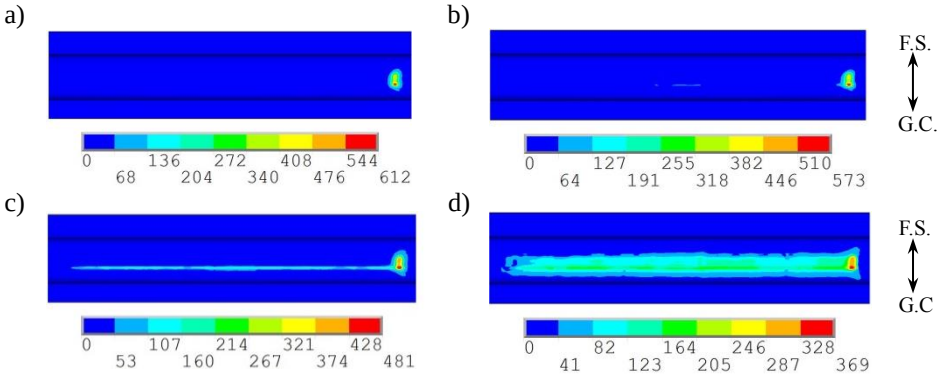

Figure 30. Top view of the rail running band variation (Unit: MPa). a) Infinite; b) 680MPa. c) 480MPa; d) 280MPa.

Figure 31 depicts the sliced plots at “AA” cutting planes, where the residual stresses located on the sub-surface are witnessed. The depth of the stressed zone is increasing from null at the case of elastic material to one or two millimeters when the yield limit is reduced to 280MPa. It should be noted that the plots are captured at the moment when the wheel runs to the end of the refined potential contact area along the rail. The regions with high stress concentration at the right side of each plot shown in Figure 30 and Figure 31 are the area, where the wheel is standing on the top of the rail.

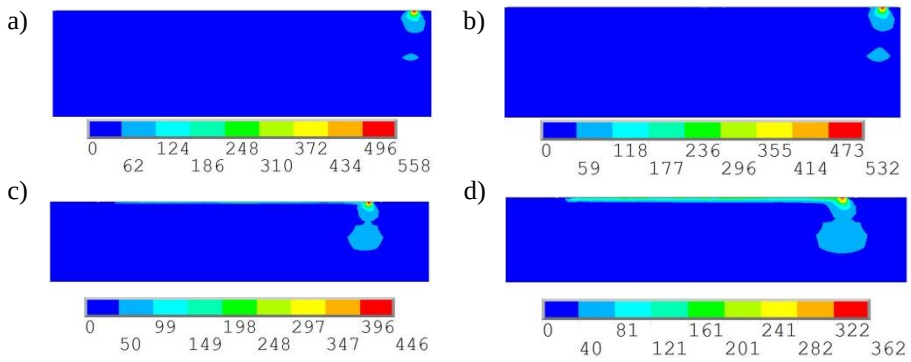

Figure 31. Sub-surface stress sliced plots at AA cutting plane (Unit: MPa). a) Infinite; b) 680MPa; c) 480MPa; d) 280MPa.

It can be concluded from the results that the width and depth of the remained residual stress zone maintains a steady rise with the decrement of the yield strength. The advantage of the FE approach, which can completely consider the elasticity of the material response, has been further demonstrated by the parametric study on the material properties.

5 Discussions

The verification of the FE model against CONTACT has been presented in the previous sections. As there are no experimental validations reported, the future work on how to validate the proposed approach is discussed in this section. Also, the further applications of the developed explicit FE model onto the complicated practical problems (such as degraded adhesion, squats, wear, etc.) are presented.

5.1 Future experimental validations

Due to the relatively small size of the contact patch (around 100mm^2) and extremely high contact stresses, it is still a challenge to measure the contact properties experimentally [8] and further validate the FE model.

To address such a challenge, considerable efforts have been made on devising new methods/devices during the last decades. For instance, in [11, 40, 41], an ultrasonic non-invasive method was successfully used to estimate the dimension of the contact patch and the resulting normal pressure in the laboratory test. Also, several on-board [10, 42, 43] and trackside [44] field measurement devices were developed to predict the wheel-rail contact forces and/or the accelerations. These experimental devices were mounted onto the wheel, bogie, axle box or rail to record the real-time signal as the wheel travelling over the rail.

In future work, there are two ways of validating the proposed FE model experimentally as inspired by the abovementioned research progress, namely:

1) Laboratory test: using the ultrasonic technique to validate the normal contact properties (i.e., contact patch and pressure) obtained from FE simulations against the measured ones;
2) Field measurement: using the on-board and/or track-side measurement systems to compare the dynamic contact forces and/or the accelerations [43] of the wheel/rail with the ones obtained from FE simulations.

5.2 Further applications of the model

One of the main advantages of the FE model is that using it the detailed stress/strain data in the contact area can be obtained, which makes it attractive to use the FE model in the advanced application wherein such information is needed. Since the FE modelling procedure (See Figure 3) has been parameterised using MATLAB scripts and ANSYS Parametric Design Language (APDL), the developed FE model can easily be adjusted and further extended to study the much complicated cases of wheel-rail interaction (e.g. worn wheel and/or rail profiles, wheel-insulated joint interaction [6] and wheel-crossing interaction [33]). Also, the FE model could be used as a tool for wheel and/or rail profile design [39] and optimisation [45, 46].

In this study, the effect of the varying operational patterns (e.g., the different friction coefficients, traction coefficients) on the tribological behaviour of wheel-rail interaction has been demonstrated. For the other critical operational conditions, for instance, the degraded adhesion [47, 48] and the presence of contaminants [49], the developed FE model can also be employed to investigate their influence on the performance of the transient wheel-rolling contact by tuning the velocity dependent friction coefficient [50].

In the present FE model, the wheel and rail interface are modelled with an uniform level surface and have no defects. In future work, the FE model could be used to model the high frequency impact in the presence of surface defects, such as squats [13], corrugations and wheel flats by introducing single or multiple artificial semi-spherical/semi-ellipsoidal irregularities on the rail/wheel surfaces. Also, since only one wheel passage is considered in the FE model, the influence of the cyclic loading on the contact properties is not included. The corresponding degradation mechanism of the surface damages, such as wear [51], rolling contact fatigue (RCF) crack initiation and propagation [52, 53], can be simulated by considering multiple wheel passages.

In order to maintain an efficient and detailed contact solution, the rail is modelled within a couple of meters and only half wheelset is considered in the present FE model. The global dynamic response of the vehicle-track interaction is neglected. In future work, a multiscale modelling approach[16, 54] (as shown in Figure 32), in which the FE model would be included as a nice component, ranging from micrometre to kilometre scales would be developed and used to study the vehicle and track interaction comprehensively. More details about the interface handshaking mechanisms of the integrated multiscale modelling approach can be found in [54].

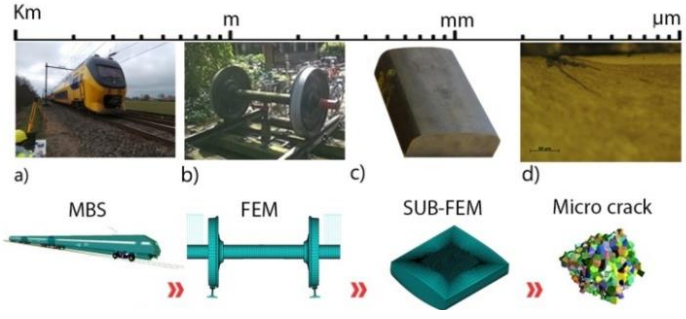

Figure 32. Schematic graph of multi-scale strategy for wheel-rail interaction [54]. a) Complete macro scale –vehicle/track

interaction; b) Component macro scale – FE model of wheel/rail interaction; c) Mesoscale – Rail FE sub-model crack initiation analysis; d) Micro scale – Rail micro-crack analysis.

6 Conclusions

In this paper the accuracy of the developed explicit FE model has been verified. Also, the effect of the operational patterns such as the friction coefficients, traction forces, contact points, etc. on the tribological behaviour of the wheel-rail interaction has been studied. The future work on the experimental validations and further applications of the developed FE model has been discussed. Based on the results and discussions of this study, the following conclusions have been drawn:

1) The integrating procedure of FE modelling verification against CONTACT have been introduced with application to the analysis of wheel-rail interaction. Using this procedure, the same conditions used in both FE and CONTACT simulations can be assured. Also, the correctness of the verification can be guaranteed. The usefulness and flexibility of such an integrating procedure have been demonstrated in the parametric study with different operational patterns (such as friction coefficient, traction force, contact point, etc.).

2) The results obtained from the CONTACT and FE analysis, including the contact pressure, shear stress, etc. agree well. Yet, tolerable discrepancies between these results still exist. The sources of the discrepancies have been explained and categorised into different groups, such as the different analysis types, solving procedures, etc. The main result of this verification is that the discrepancy between the results of CONTACT and FEM is reasonable enough for the FEM to be used in the future research. However, as one major disadvantage of FE analysis, it should be mentioned that the computational expenses of the present FE simulation (around 10 hours) are much higher than the ones of CONTACT simulation (2~3 minutes). As for the cases of contact model verification (e.g., newly developed FE model or other sophisticated models), the programme of CONTACT is recommended.

3) The changes of the friction coefficient, the braking and accelerating operation as well as the location of the contact point can bring about a significant influence on the tribological response in the wheel and rail interaction, such as the distribution of normal pressure, shear stress, slip-adhesion area as well as the subsurface stress. The accuracy of the corresponding FE simulations under varying operational parameters has been verified by comparing it with the one of CONTACT.

4) As one of the most pronounced advantages of the FE method, the consideration of plasticity in the material models will drastically reduce the magnitude of the shear stress and contact pressure. Also, the residual stress zone is observed at the distance of 1~2mm under the surface along wheel travelling path. The lower the material yield strength limit is, the wider and deeper the residual stress zone will be.

Acknowledgement

The authors are very grateful to all the reviewers for their thorough reading of the manuscript and their constructive comments on it.

References

[1] S. R. Wu and L. Gu, *Introduction to the explicit finite element method for nonlinear transient dynamics*. John Wiley & Sons, 2012.

[2] W. L. Oberkampf and T. G. Trucano, "Verification and validation in computational fluid dynamics," *Progress in Aerospace Sciences,* vol. 38, no. 3, pp. 209-272, 4// 2002.

[3] C. L. Pun, Q. Kan, P. J. Mutton, G. Kang, and W. Yan, "An efficient computational approach to evaluate the ratcheting performance of rail steels under cyclic rolling contact in service," *International Journal of Mechanical Sciences,* vol. 101-102, pp. 214-226, 10// 2015.

[4] C. L. Pun, Q. Kan, P. J. Mutton, G. Kang, and W. Yan, "Ratcheting Behaviour of High Strength Rail Steels under Bi-axial Compression-Torsion Loadings: Experiment and Simulation," *International Journal of Fatigue,* no. 0, 2014.

[5] K. D. Vo, A. K. Tieu, H. T. Zhu, and P. B. Kosasih, "A 3D dynamic model to investigate wheel–rail contact under high and low adhesion," *International Journal of Mechanical Sciences,* vol. 85, pp. 63-75, 2014.

[6] N. K. Mandal and M. Dhanasekar, "Sub-modelling for the ratchetting failure of insulated rail joints," (in English), *International Journal of Mechanical Sciences,* vol. 75, pp. 110-122, Oct 2013.

[7] H. Doi, T. Miyamoto, Y. Nishiyama, S. Ohe, and H. Kamachi, "A new experimental device to investigate creep forces between wheel and rail," (in English), *Wear,* vol. 271, no. 1-2, pp. 40-46, May 18 2011.

[8] X. Zhao and Z. Li, "The solution of frictional wheel–rail rolling contact with a 3D transient finite element model: Validation and error analysis," *Wear,* vol. 271, no. 1-2, pp. 444-452, 5/18/ 2011.

[9] X. Deng, Z. Qian, and R. Dollevoet, "Lagrangian Explicit Finite Element Modeling for Spin-Rolling Contact," *Journal of Tribology,* vol. 137, no. 4, p. 041401, 2015.

[10] A. Matsumoto *et al.*, "A new measuring method of wheel–rail contact forces and related considerations," *Wear,* vol. 265, no. 9-10, pp. 1518-1525, 2008.

[11] M. Pau, F. Aymerich, and F. Ginesu, "Distribution of contact pressure in wheel–rail contact area," *Wear,* vol. 253, no. 1-2, pp. 265-274, 7// 2002.

[12] E. A. H. Vollebregt, S. D. Iwnicki, G. Xie, and P. Shackleton, "Assessing the accuracy of different simplified frictional rolling contact algorithms," *Vehicle System Dynamics,* vol. 50, no. 1, pp. 1-17, 2012/01/01 2012.

[13] Z. Li, X. Zhao, C. Esveld, R. Dollevoet, and M. Molodova, "An investigation into the causes of squats—Correlation analysis and numerical modeling," *Wear,* vol. 265, no. 9-10, pp. 1349-1355, 10/30/ 2008.

[14] O. Polach, "A fast wheel-rail forces calculation computer code," (in English), *Dynamics of Vehicles on Roads and on Tracks,* vol. 33, pp. 728-739, 2000.

[15] O. Polach, "Creep forces in simulations of traction vehicles running on adhesion limit," *Wear,* vol. 258, no. 7, pp. 992-1000, 2005.

[16] M. Wiest, E. Kassa, W. Daves, J. C. O. Nielsen, and H. Ossberger, "Assessment of methods for calculating contact pressure in wheel-rail/switch contact," *Wear,* vol. 265, no. 9–10, pp. 1439-1445, 10/30/ 2008.

[17] E. Olsson and P. L. Larsson, "On the tangential contact behavior at elastic–plastic spherical contact problems," *Wear,* vol. 319, no. 1–2, pp. 110-117, 11/15/ 2014.

[18] E. E. Magel and Y. Liu, "On some aspects of the wheel/rail interaction," *Wear,* no. 0, 2013.

[19] X. Liu and P. A. Meehan, "Investigation of the effect of relative humidity on lateral force in rolling contact and curve squeal," *Wear,* vol. 310, no. 1-2, pp. 12-19, 2/15/ 2014.

[20] S. R. Lewis, R. Lewis, and U. Olofsson, "An alternative method for the assessment of railhead traction," (in English), *Wear,* vol. 271, no. 1-2, pp. 62-70, May 18 2011.

[21] H. Kanehara and T. Fujioka, "Measuring rail/wheel contact points of running railway vehicles," *Wear,* vol. 253, no. 1-2, pp. 275-283, 2002.

[22] Y. Ma and V. L. Markine, "A Numerical Procedure for Analysis of W/R Contact Using Explicit Finite Element Methods," presented at the 10th International Conference on Contact Mechanics, Colorado Springs, CO. USA 2015.

[23] J. O. Hallquist, G. L. Goudreau, and D. J. Benson, "Sliding Interfaces with Contact-Impact in Large-Scale Lagrangian Computations," (in English), *Computer Methods in Applied Mechanics and Engineering,* vol. 51, no. 1-3, pp. 107-137, 1985.

[24] J. Hallquist, "ANSYS/LS-DYNA Theoretical Manual [M]," *Livermore Software Technology Corporation, USA,* 2005.

[25] D. J. Benson and J. O. Hallquist, "A single surface contact algorithm for the post-buckling analysis of shell structures," *Computer Methods in Applied Mechanics and Engineering,* vol. 78, no. 2, pp. 141-

163, 1// 1990.
[26] J. J. Kalker, *Three-dimensional elastic bodies in rolling contact*. Springer Science & Business Media, 1990.
[27] E. Vollebregt, "User guide for CONTACT, JJ Kalker's variational contact model," *Delft,, The Netherlands Tech. Rep. TR09-03, VORtech BV Available at www. kalkersoftware. org,* 2009.
[28] J. Piotrowski and W. Kik, "A simplified model of wheel/rail contact mechanics for non-Hertzian problems and its application in rail vehicle dynamic simulations," *Vehicle System Dynamics,* vol. 46, no. 1-2, pp. 27-48, 2008.
[29] G. Duvaut and J.-L. Lions, "inequations en mecanique et en physique.[Les]," 1976.
[30] J. Kalker, "Contact mechanical algorithms," *Communications in applied numerical methods,* vol. 4, no. 1, pp. 25-32, 1988.
[31] Z. Li, "Wheel - Rail Rolling Contact and Its Application to Wear Simulation," PhD, Delft University of Technology, 2002.
[32] E. Vollebregt and G. Segal, "Solving conformal wheel–rail rolling contact problems," *Vehicle System Dynamics,* vol. 52, no. sup1, pp. 455-468, 2014/05/30 2014.
[33] Y. Ma, A. A. Mashal, and V. L. Markine, "Numerical Analysis of Wheel-Crossing Interaction Using a Coupling Strategy," presented at the The Third International Conference on Railway Technology: Research, Development and Maintenance, Cagliari, Sardinia, Italy 2016.
[34] Y. Ma, M. Ren, G. Hu, and C. Tian, "Optimal analysis on rail pre-grinding profile in high-speed railway," *Chinese Journal of Mechanical Engineering,* vol. 48, no. 8, pp. 90-97, 2012.
[35] N. Hu, "A solution method for dynamic contact problems," *Computers & Structures,* vol. 63, no. 6, pp. 1053-1063, 6// 1997.
[36] I. Huněk, "On a penalty formulation for contact-impact problems," *Computers & Structures,* vol. 48, no. 2, pp. 193-203, 1993/07/17 1993.
[37] Z.-H. Zhong and J. Mackerle, "Contact-Impact Problems: A Review With Bibliography," *Applied Mechanics Reviews,* vol. 47, no. 2, pp. 55-76, 1994.
[38] Y. Ma, V. L. Markine, A. A. Mashal, and M. Ren, "Effect of Wheel-Rail Interface Parameters on Contact Stability in Explicit Finite Element Analysis," *Proceedings of the Institution of Mechanical Engineers, Part F: Journal of Rail and Rapid Transit(In revision),* 2016.
[39] R. P. B. J. Dollevoet, *Design of an Anti Head Check profile based on stress relief*. University of Twente, 2010.
[40] M. Pau and B. Leban, "Ultrasonic assessment of wheel—rail contact evolution exposed to artificially induced wear," *Proceedings of the Institution of Mechanical Engineers, Part F: Journal of Rail and Rapid Transit,* vol. 223, no. 4, pp. 353-364, July 1, 2009 2009.
[41] M. B. Marshall, R. Lewis, R. S. Dwyer-Joyce, U. Olofsson, and S. Björklund, "Experimental Characterization of Wheel-Rail Contact Patch Evolution," *Journal of Tribology,* vol. 128, no. 3, p. 493, 2006.
[42] P. Gullers, L. Andersson, and R. Lundén, "High-frequency vertical wheel–rail contact forces—Field measurements and influence of track irregularities," *Wear,* vol. 265, no. 9-10, pp. 1472-1478, 10/30/ 2008.
[43] M. Molodova, Z. Li, A. Núñez, and R. Dollevoet, "Validation of a finite element model for axle box acceleration at squats in the high frequency range," *Computers & Structures,* vol. 141, pp. 84-93, 8// 2014.
[44] X. Liu and V. Markine, "Dynamic experimental tools for condition monitoring of railway turnout crossing," presented at the The Ninth International Conference on Engineering Computational Technology, 2014.
[45] I. Y. Shevtsov, V. L. Markine, and C. Esveld, "Optimal design of wheel profile for railway vehicles," (in English), *Wear,* vol. 258, no. 7-8, pp. 1022-1030, Mar 2005.
[46] C. Wan, V. Markine, and R. Dollevoet, "Robust optimisation of railway crossing geometry," *Vehicle System Dynamics,* pp. 1-21, 2016.
[47] E. Meli and A. Ridolfi, "An innovative wheel–rail contact model for railway vehicles under degraded adhesion conditions," *Multibody System Dynamics,* journal article vol. 33, no. 3, pp. 285-313, 2015.
[48] E. Meli, L. Pugi, and A. Ridolfi, "An innovative degraded adhesion model for multibody applications in the railway field," *Multibody System Dynamics,* journal article vol. 32, no. 2, pp. 133-157, 2014.
[49] X. Zhao, Z. F. Wen, M. H. Zhu, and X. S. Jin, "A study on high-speed rolling contact between a wheel and a contaminated rail," (in English), *Vehicle System Dynamics,* vol. 52, no. 10, pp. 1270-1287, 2014/10/03 2014.
[50] X. Zhao and Z. Li, "Three dimensional finite element solution of wheel-rail rolling contact with velocity dependent," in *Proceedings of 9th International Conference on Contact Mechanics and Wear of Rail/Wheel Systems (CM2012),*, Chengdu, China, 2012.

[51] P. J. Blau, "Embedding Wear Models into Friction Models," *Tribology Letters,* journal article vol. 34, no. 1, pp. 75-79, 2009.
[52] Y. Ma and V. L. Markine, "Numerical Analysis for Fatigue Life Prediction on Railroad RCF Crack Initiation," presented at the 10th International Conference on Contact Mechanics, Colorado, 2015.
[53] Y. Ma, V. L. Markine, and A. A. Mashal, "Numerical Analysis of Rail Surface Crack Propagation Under Cyclic Rolling-Sliding Contact Loads," presented at the The Third International Conference on Railway Technology: Research, Development and Maintenance, Cagliari, Sardinia, Italy 2016.
[54] Y. Ma, V. L. Markine, and A. A. Mashal, "Rail surface crack initiation analysis using multi-scale coupling approach," presented at the 24th international symposium on dynamics of vehicles on roads and tracks, Graz, 2015.